

Gaussian Splatting with Discretized SDF for Relightable Assets

Zuo-Liang Zhu¹ Jian Yang^{1†} Beibei Wang^{2†}

¹Nankai University ²Nanjing University

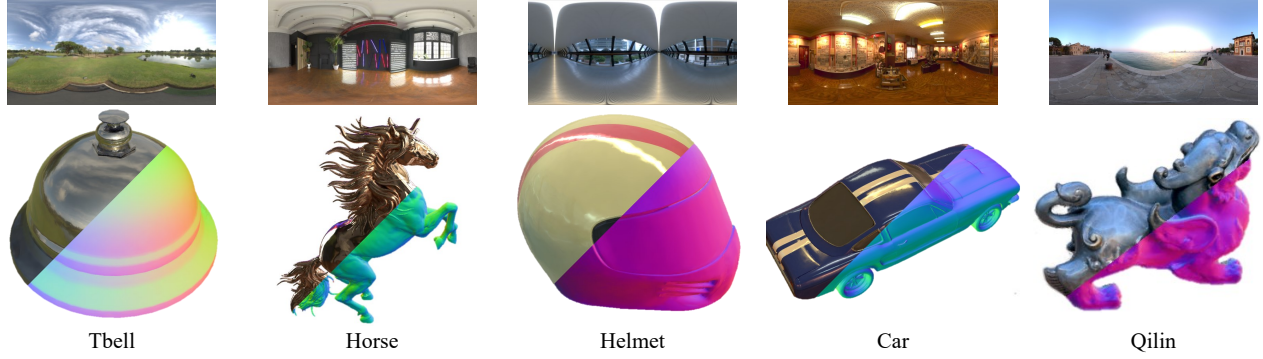


Figure 1. We present a relightable Gaussian splatting framework that introduces a discretized SDF to promote decomposition quality. We show five relighting results (left) and their normal estimation (right), including ‘Tbell’ and ‘Horse’ from NeRO [17], ‘Helmet’ and ‘Car’ from Ref-NeRF [26], and ‘Qilin’ from NeILF++ [37], where ‘Qilin’ is a real scene. Our method demonstrates a robust decomposition of geometry and material for various objects, leading to photo-realistic object relighting.

Abstract

3D Gaussian splatting (3DGS) has shown its detailed expressive ability and highly efficient rendering speed in the novel view synthesis (NVS) task. The application to inverse rendering still faces several challenges, as the discrete nature of Gaussian primitives makes it difficult to apply geometry constraints. Recent works introduce the signed distance field (SDF) as an extra continuous representation to regularize the geometry defined by Gaussian primitives. It improves the decomposition quality, at the cost of increasing memory usage and complicating training. Unlike these works, we introduce a **discretized SDF** to represent the continuous SDF in a discrete manner by encoding it within each Gaussian using a sampled value. This approach allows us to link the SDF with the Gaussian opacity through an SDF-to-opacity transformation, enabling rendering the SDF via splatting and avoiding the computational cost of ray marching. The key challenge is to regularize the discrete samples to be consistent with the underlying SDF, as the discrete representation can hardly apply the gradient-based constraints (e.g., Eikonal loss). For this, we project

Gaussians onto the zero-level set of SDF and enforce alignment with the surface from splatting, namely a projection-based consistency loss. Thanks to the discretized SDF, our method achieves higher relighting quality, while requiring no extra memory beyond GS and avoiding complex manually designed optimization. The experiments reveal that our method outperforms existing Gaussian-based inverse rendering methods. Our code is available at <https://github.com/NK-CS-ZZL/DiscretizedSDF>.

1. Introduction

While creating relightable 3D assets from multi-view images is valuable for many downstream tasks (e.g., augmented reality, virtual reality), it is challenging due to the ambiguity from decomposing geometry, material, and light.

A key point for decomposing these factors is the regularization of geometry, as high-quality geometry is the prerequisite to estimate reasonable material and light. The signed distance field (SDF) has been introduced into neural radiance field (NeRF) [21] as an effective geometric prior, as NeuS [28]. Due to SDF constraints, several methods [14, 25, 42] have shown a robust decomposition of geometry and material. Unfortunately, these methods require long training and rendering time, due to the expensive ray-

[†]Corresponding author.

¹PCA Lab, VCIP, College of Computer Science, Nankai University

²School of Intelligence Science and Technology, Nanjing University, Suzhou, China.

marching operation. More recently, 3D Gaussian splatting (3DGS) [12] achieves more detailed appearance modeling while enabling real-time rendering and fast training. It has also been introduced into inverse rendering [6, 9, 16, 44]. However, the decomposition in the GS framework becomes more problematic, due to insufficient geometric constraints. Several works [32, 35, 41, 44] optimize an extra SDF network with Gaussians jointly for geometry regularization. While these designs improve the geometry quality, they increase the memory usage and require complex optimization strategies (*e.g.*, warm-up [35], or multi-stage training [44]) to balance two representations.

In this paper, we introduce a *discretized SDF* to represent the continuous SDF in a discrete manner by encoding it within each Gaussian using a sampled value. This design enables effective geometry regularization in Gaussian-based relighting frameworks while maintaining simplicity and memory efficiency. We link the SDF with the Gaussian opacity through an SDF-to-opacity transformation, allowing rendering the SDF via splatting and avoiding the computational cost of ray marching. The key problem is to regularize SDF with the discrete samples, as the gradient-based losses used to regularize SDF (*e.g.*, Eikonal loss [7]) are unfeasible for the discrete samples. For this, we project Gaussians onto the zero-level set of SDF and enforce alignment with the surface from splatting, namely projection-based consistency loss, proven to be an approximation of the Eikonal loss. This way, we unify the representation between SDF and Gaussian, benefiting from the flexibility of the Gaussian primitive and the robustness of SDF while maintaining simplicity, without introducing extra representation. Besides, inspired by previous SDF works [28, 33], we propose a spherical initialization tailored for Gaussian splatting, which avoids falling into local minima and improves the robustness of the model.

As a result, our method provides high-quality and robust decomposition for objects across various materials, enables realistic relighting with only 20% of memory usage compared to previous methods [44], and simplifies the optimization process, thanks to the unified representation. In summary, our main contributions include

- a novel regularization in the GS framework with a discretized SDF to improve decomposition quality,
- a projection-based loss to regularize discretized SDF, proven as an approximation of the Eikonal loss, and
- extensive experiments show our method outperforms existing Gaussian-based methods with diverse metrics.

2. Related works

2.1. Inverse rendering

Inverse rendering aims to decompose geometry, material, and light from multi-view RGB images. One group of meth-

ods adopts the geometry formulation from NeRF [21] in a density [3, 4, 10, 24] or SDF manner [2, 25, 27, 38, 39, 42]. Due to the well-constrained geometry of the SDF, SDF-based methods can decompose the material and geometry robustly. Especially, NeRO [17] can handle challenging reflective objects by explicitly integrating the rendering equation. TensoSDF [14] uses roughness-aware integration of radiance and reflectance fields to manage diverse materials. However, these methods rely on expensive ray marching and suffer from slow training speed with high memory usage in training. Unlike prior works, our discretized SDF ensures robust decomposition across various materials, while maintaining a fast training speed and low memory costs.

More recently, Gaussian-based inverse rendering methods have emerged. These methods regularize geometry from Gaussians variously. GShader [9] and GIR [23] link the shortest axis of Gaussian with the normal. GShader, R3DG [6], and GS-IR [16] introduce a loss to align the Gaussian normal with the depth-derived one. Later, SDF is introduced into this field to regularize geometry. DeferredGS [32] distills the normal from the pretrained SDF to refine the normal from Gaussians. GS-ROR [44] utilizes the normal and depth as a bridge to optimize the Gaussian and SDF jointly. However, introducing an extra SDF network makes the model larger and harder to optimize.

Instead of using additional continuous representation for SDF, our work aims to directly encode discrete values of SDF samples on Gaussian primitives and regularize the geometry via this discretized SDF. In this way, our framework benefits from both GS and SDF within a unified representation, leading to a more lightweight and efficient model.

2.2. Learning SDF from multi-view images

SDF is a fundamental surface representation [19] adopted by various tasks (*e.g.*, surface reconstruction, inverse rendering). Particularly, NeuS [28] that links the SDF with the density in NeRF [21] became mainstream for learning SDF from multi-view images. In their framework, the SDF is stored by multi-layer perceptrons [33, 36] or grid-like representations [14, 15, 22, 29], which is continuous and convenient to obtain the gradient to regularize the SDF [7, 31, 36].

Recently, 3DGS [12] became a new framework for the multi-view stereo, providing impressive real-time novel view synthesis (NVS) results. However, due to its discrete nature, reconstructing an accurate and continuous surface is challenging. To address this, some works optimize the SDF with 3DGS jointly. NeuSG [5] align the SDF gradient with the Gaussian normal. 3DGSR [18] builds an SDF-to-opacity transformation and regularizes the depth along with normal from Gaussians by the ones from SDF. GSDF [35] utilizes the depth from Gaussians to accelerate the sampling and manipulate densifying/pruning via SDF. GS-Pull [41] introduces the pulling operation to align the zero-level set

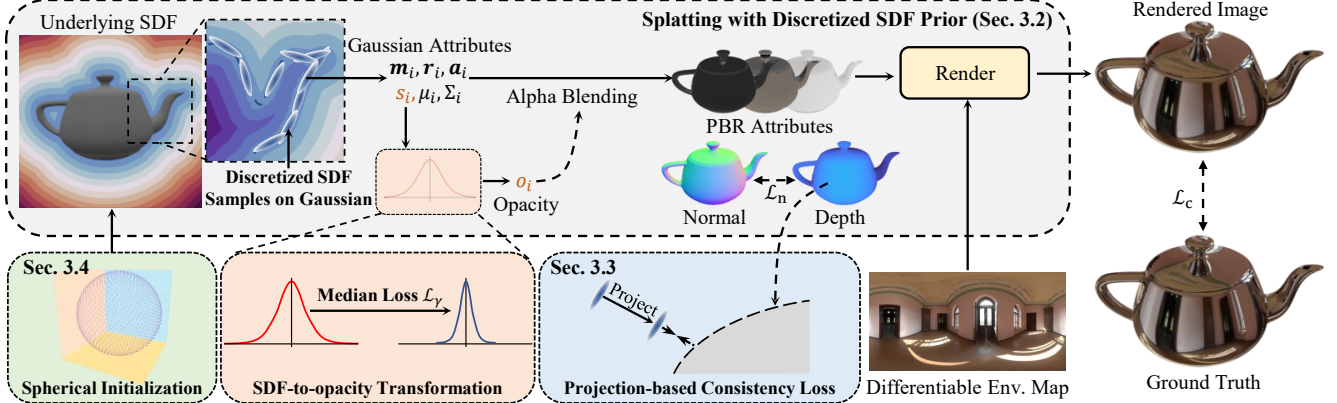


Figure 2. Overview of our framework. Our model discretizes the underlying continuous SDF into discrete samples and encodes the SDF values of samples on Gaussian primitives. We propose the median loss to facilitate convergence and projection-based consistency loss to regularize the discrete values of SDF samples. Besides, we design a spherical initialization for foreground objects to avoid local minima.

and the Gaussian position for an accurate surface. All previous works utilize an extra representation while our work employs a single representation that uses Gaussian primitives as discrete samples from SDF to regularize geometry.

3. Method

In this section, we briefly review Gaussian splatting (Sec. 3.1) and propose a discretized SDF within the Gaussian splatting framework for inverse rendering (Sec. 3.2). Then, we present a projection-based loss to constrain the geometry when common gradient-based regularization becomes unfeasible for the discrete representation (Sec. 3.3). Finally, we propose a spherical initialization to avoid the geometry trapping into local minima (Sec. 3.4).

3.1. Preliminaries

2DGS. 2DGS [8] flattens the Gaussian primitive into a 2D disk defined by two tangent vectors (t_u, t_v) and their corresponding scaling (s_u, s_v), whose normal is $n = t_u \times t_v$. They compute the ray-Gaussian response α_i by a ray-splat intersection and follow the rendering pipeline in 3DGS as:

$$C = \sum_{i=0}^n c_i \alpha_i \prod_{j=1}^{i-1} (1 - \alpha_j), \quad (1)$$

where c_i, α_i is the color and the ray-Gaussian response.

Relightable Gaussian splatting. To enable relighting, the color of Gaussian is replaced by physically based rendering (PBR) attributes (e.g., albedo, roughness). Two existing pipelines differ in the order of blending and evaluating the rendering equation, namely forward and deferred shading. The forward one renders the color for each Gaussian and blends them, while the deferred one blends the PBR attributes first and renders each pixel.

3.2. Relightable GS with a discretized SDF

Previous works [34, 35, 41] introduced an extra SDF representation (e.g., a network) into the GS framework as geometry constraints to improve decomposition quality, leading to higher memory costs and more complex optimization strategies. Hence, the main question is how to unify the Gaussian primitive and the SDF to avoid these drawbacks. To this end, we propose the discretized SDF into the Gaussian splatting as a geometry prior, as shown in Fig. 2.

We first describe our baseline solution and introduce our discretized SDF. Our framework is built on 2DGS [8] with the deferred shading, as the 2D Gaussian is robust for geometry [8] and deferred shading is more stable across diverse materials [32, 44]. Besides, we choose the Principled Bidirectional Reflectance Distribution Function (BRDF) [20] with split-sum approximation [11] as our shading model.

Next, we propose the discretized SDF into our framework. Instead of using an extra representation for SDF, we encode an SDF value on the Gaussian as an extra attribute, besides PBR attributes, scaling, and quaternion. Then, the opacity in each Gaussian is derived from the SDF value via an SDF-to-opacity transformation.

$$o_i = \mathcal{T}_\gamma(s_i) = \frac{4 \cdot e^{-\gamma s_i}}{(1 + e^{-\gamma s_i})^2}, \quad (2)$$

where o_i is the opacity, s_i is the SDF value of i -th Gaussian, and γ is a global learnable parameter to control the variance of the transformation. Note that the opacity of each Gaussian is computed from the SDF, rather than directly learned. With the transformation, Gaussians can be splatted the same as in previous works [8, 18], and the Gaussian attributes together with the parameter of the transformation can be optimized. However, we observe a slow convergence, as the joint optimization of the transformation parameter γ and the SDF value s_i spans a large search space.

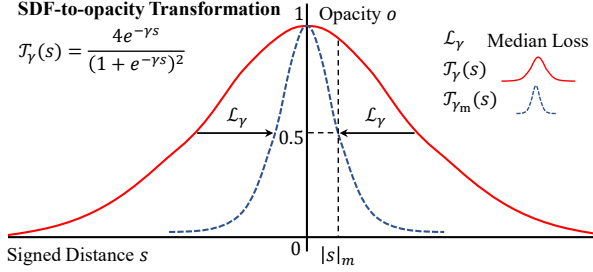


Figure 3. The SDF-to-opacity transformation \mathcal{T}_γ for splatting is a bell-shaped function ranging from zero to one. The proposed median loss \mathcal{L}_γ drags \mathcal{T}_γ (red line) to narrower \mathcal{T}_{γ_m} (blue line).

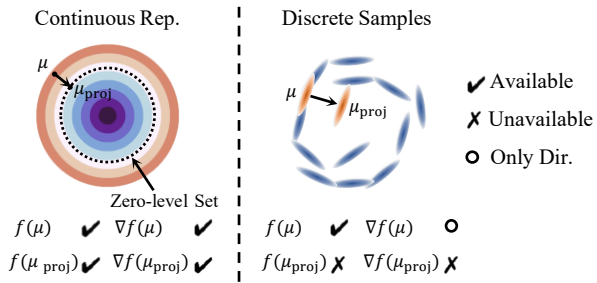


Figure 4. The difference between continuous and discretized SDF in regularization. For discrete samples, we can only obtain the gradient direction of SDF¹, so the Eikonal loss is infeasible. Besides, since discretized SDF does not support the query of SDF value at the projected point, we cannot constrain projected points on the surface directly and thus use depth as a bridge to achieve that.

To mitigate the challenges in the joint learning of γ and s_i , we found the median of unsigned distance $|s|_m$ across all Gaussian primitives is an effective indicator for convergence. Specifically, a high opacity $o_m = \mathcal{T}_{\gamma_m}(|s|_m)$ at the median distance indicates the transformation should be narrowed, as shown in Fig. 3. Hence, we link the transformation parameter to the median $|s|_m$ and empirically encourage the opacity o_m below 0.5. Accordingly, we derive γ_m from $\mathcal{T}_{\gamma_m}(|s|_m) = 0.5$ to meet this condition:

$$\gamma_m = -\frac{\log(3 - 2\sqrt{2})}{|s|_m}, \quad (3)$$

which is used to guide the transformation parameter γ with our proposed *SDF-to-opacity transformation median loss*:

$$\mathcal{L}_\gamma = \max(\gamma_m - \gamma, 0). \quad (4)$$

Note that, γ_m is used as a guide of γ to quickly narrow the transformation. After it reaches \mathcal{T}_{γ_m} defined by γ_m , we do not force the transformation \mathcal{T}_γ identical to \mathcal{T}_{γ_m} and allow

¹An ideal SDF has a gradient magnitude of one, which does not hold during optimization, and discrete-sample magnitudes cannot be directly measured. Thus, only the direction on Gaussian is accessible.

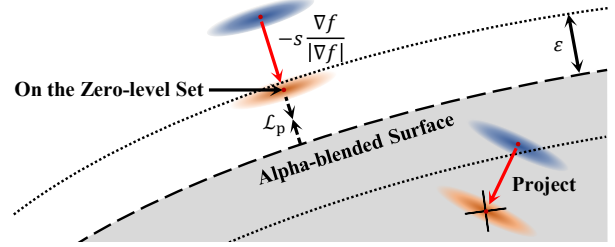


Figure 5. The projection-based consistency loss minimizes the difference between the zero-level set of SDF and the alpha-blended surface defined by Gaussians. The exceptional Gaussians whose difference is larger than ϵ are discarded.

it to be sharper. In this way, the Gaussians can quickly approach the surface and converge into a sharp distribution.

3.3. Projection-based consistency loss

A signed distance function f meets the Eikonal condition $|\nabla f| = 1$, indicating the gradient magnitude to position should be constantly one, which is usually used to constrain an implicit SDF, as the gradient ∇f can be computed easily from a continuous SDF. However, it is unclear how to obtain it for SDF samples encoded on Gaussians. As shown in Fig. 4, only the gradient direction on Gaussian is available, which is the normal direction $n = \frac{\nabla f}{|\nabla f|} = t_u \times t_v$. Inspired by Neural-Pull [1], we design a new constraint for the SDF samples tailored with Gaussians by projecting Gaussians to the surface defined by the zero-level set, enforcing the consistency between the projected point and alpha-blended surface defined by Gaussians, namely *projection-based consistency loss*, proven to be an approximation of the Eikonal condition. Note that although our design shares a similar theory with Neural-Pull, we do not use an extra network for SDF and have no ground-truth point cloud as supervision. Specifically, we project a Gaussian g_i onto the zero-level set, leading to a projected point μ_{proj} :

$$\mu_{proj} = \mu_i - s_i \frac{\nabla f_i}{|\nabla f_i|}, \quad (5)$$

where $\mu_i, s_i, \nabla f_i$ are the position, SDF value and SDF gradient of g_i , respectively. The projected point should align with the alpha-blended surface from Gaussians. For this, we ensure this property by minimizing their difference. Here, we use depth rather than position, due to simplicity, leading to the following difference $\epsilon_{proj} = |D_{agg} - D_{proj}|$ where D_{agg} is the alpha-blended or aggregated depth, and D_{proj} is the depth of projected point μ_{proj} under the same view.

This difference can not be used as the loss directly, as some exceptional Gaussians should be discarded. One case is that some Gaussians belong to occluded surfaces or objects in the current view. The other case is that non-differentiable regions (such as self-intersection [19]) might

	GShader	GS-IR	R3DG	GS-ROR	Ours
	PSNR / SSIM / LPIPS				
Angel	17.49 / 0.8336 / 0.1901	15.64 / 0.6126 / 0.1428	16.65 / 0.8013 / 0.1181	20.81 / 0.8775 / 0.0858	22.03 / 0.8919 / 0.0819
Bell	19.01 / 0.8804 / 0.5203	12.61 / 0.2807 / 0.1431	16.15 / 0.8391 / 0.1329	24.49 / 0.9267 / 0.0795	24.67 / 0.9280 / 0.0842
Cat	16.00 / 0.8642 / 0.1591	18.04 / 0.7907 / 0.1171	17.49 / 0.8503 / 0.1114	26.28 / 0.9421 / 0.0596	26.48 / 0.9374 / 0.0661
Horse	22.49 / 0.9262 / 0.1606	17.40 / 0.7270 / 0.0866	20.63 / 0.8832 / 0.0498	23.31 / 0.9376 / 0.0356	24.01 / 0.9481 / 0.0351
Luyu	15.62 / 0.8254 / 0.1391	19.00 / 0.7727 / 0.1094	17.47 / 0.8168 / 0.1057	22.61 / 0.8995 / 0.0672	23.80 / 0.9017 / 0.0699
Potion	12.33 / 0.7575 / 0.2142	16.37 / 0.7051 / 0.1614	14.99 / 0.7799 / 0.1832	25.67 / 0.9175 / 0.0937	27.31 / 0.9280 / 0.0982
Tbell	14.42 / 0.8007 / 0.3368	14.35 / 0.5419 / 0.1970	15.99 / 0.7965 / 0.1877	22.80 / 0.9180 / 0.0953	23.66 / 0.9191 / 0.0981
Teapot	18.21 / 0.8560 / 0.1716	16.63 / 0.7646 / 0.1312	17.36 / 0.8389 / 0.1194	21.17 / 0.8932 / 0.0982	24.19 / 0.9293 / 0.0760
Mean	16.95 / 0.8430 / 0.2365	16.26 / 0.6494 / 0.1361	17.09 / 0.8258 / 0.1260	23.39 / 0.9140 / 0.0769	24.52 / 0.9229 / 0.0762
Training	0.5h	0.5h	1h	1.5h	1h
Ren. FPS	50	214	50	208	143
Memory	4G	8G	20G	22G	4G

Table 1. The quantitative comparison with Gaussian-based methods on the Glossy Blender dataset in terms of PSNR↑, SSIM↑, and LPIPS↓. Numbers in red indicate the best performance, and numbers in orange indicate the second best.

	GShader	GS-IR	R3DG	GS-ROR	Ours
	PSNR / SSIM / LPIPS				
Armad.	22.86 / 0.9280 / 0.0821	28.31 / 0.9121 / 0.0591	30.76 / 0.9526 / 0.0649	31.33 / 0.9593 / 0.0482	31.05 / 0.9621 / 0.0536
Ficus	24.61 / 0.9491 / 0.0956	24.39 / 0.8762 / 0.0360	27.23 / 0.9637 / 0.0437	26.28 / 0.9542 / 0.0439	27.85 / 0.9639 / 0.0390
Hotdog	17.45 / 0.8838 / 0.1408	22.36 / 0.8931 / 0.0875	24.59 / 0.9162 / 0.1275	25.21 / 0.9307 / 0.0771	26.23 / 0.9360 / 0.0746
Lego	13.41 / 0.7904 / 0.1193	23.79 / 0.8750 / 0.0879	22.49 / 0.8682 / 0.1423	25.46 / 0.9083 / 0.0724	25.81 / 0.9087 / 0.0791
Mean	19.58 / 0.8878 / 0.1095	24.71 / 0.8891 / 0.0676	26.27 / 0.9252 / 0.0946	27.07 / 0.9381 / 0.0604	27.78 / 0.9427 / 0.0626

Table 2. The quantitative comparison with Gaussian-based methods on the TensoIR Synthetic dataset in terms of PSNR↑, SSIM↑, and LPIPS↓. Numbers in red indicate the best performance and numbers in orange indicate the second best.

lead to a huge difference ϵ_{proj} . These two cases interrupt consistency significantly. Unfortunately, it is difficult to recognize them. Therefore, we use a simple and practical solution, by assuming the difference between the two surfaces should be already close and thresholding the difference with a hyper-parameter ε , as shown in Fig. 5.

$$\mathcal{L}_p = \frac{1}{N} \sum_{i \in N} \begin{cases} \epsilon_{\text{proj}}^i, & \epsilon_{\text{proj}}^i \leq \varepsilon, \\ 0, & \epsilon_{\text{proj}}^i > \varepsilon. \end{cases} \quad (6)$$

Note that we apply this loss after 1K iterations when the coarse geometry is stable so that the assumption holds.

The theory behind the loss is an approximation of the Eikonal condition, proven in the supplementary. This loss encourages smooth reconstructed surfaces while maintaining the flexibility from Gaussian for geometry details.

3.4. Spherical initialization

We found that some erroneous geometry emerges at the early stage of training and can hardly be recovered. This indicates that the initialization makes the geometry prone to trapping into local minima. Since sphere-like initializations revealed their effect in volumetric rendering of SDF [28, 33], we design a spherical initialization of foreground objects tailored for Gaussian splatting to avoid local

minima and to encourage optimal geometry. Specifically, we employ the points uniformly sampled on a unit sphere to initialize Gaussians. The design mitigates broken surfaces and overfitting under the training appearance, further improving the geometry robustness.

4. Experiments

In this section, we present our training details (Sec. 4.1) and evaluation setup (Sec. 4.2). Then, we compare our method with the representative methods (Sec. 4.3) and conduct ablation studies on our proposed designs (Sec. 4.4).

4.1. Implementation details

We optimized our model using Adam optimizer [13] for 30,000 iterations with the loss:

$$\mathcal{L} = \mathcal{L}_c + \lambda_n \mathcal{L}_n + \lambda_d \mathcal{L}_d + \lambda_\gamma \mathcal{L}_\gamma + \lambda_p \mathcal{L}_p + \lambda_{sm} \mathcal{L}_{sm} + \lambda_m \mathcal{L}_m, \quad (7)$$

where $\lambda_{[\cdot]}$ is the corresponding weight of loss $\mathcal{L}_{[\cdot]}$. \mathcal{L}_c is the rendering loss between the rendered image and the ground truth. \mathcal{L}_n and \mathcal{L}_d are the normal consistency and the distortion loss, inheriting from 2DGS. \mathcal{L}_{sm} is a smoothness regularization for PBR attributes, and \mathcal{L}_m is the optional mask loss widely adopted by existing relighting methods [6, 38].

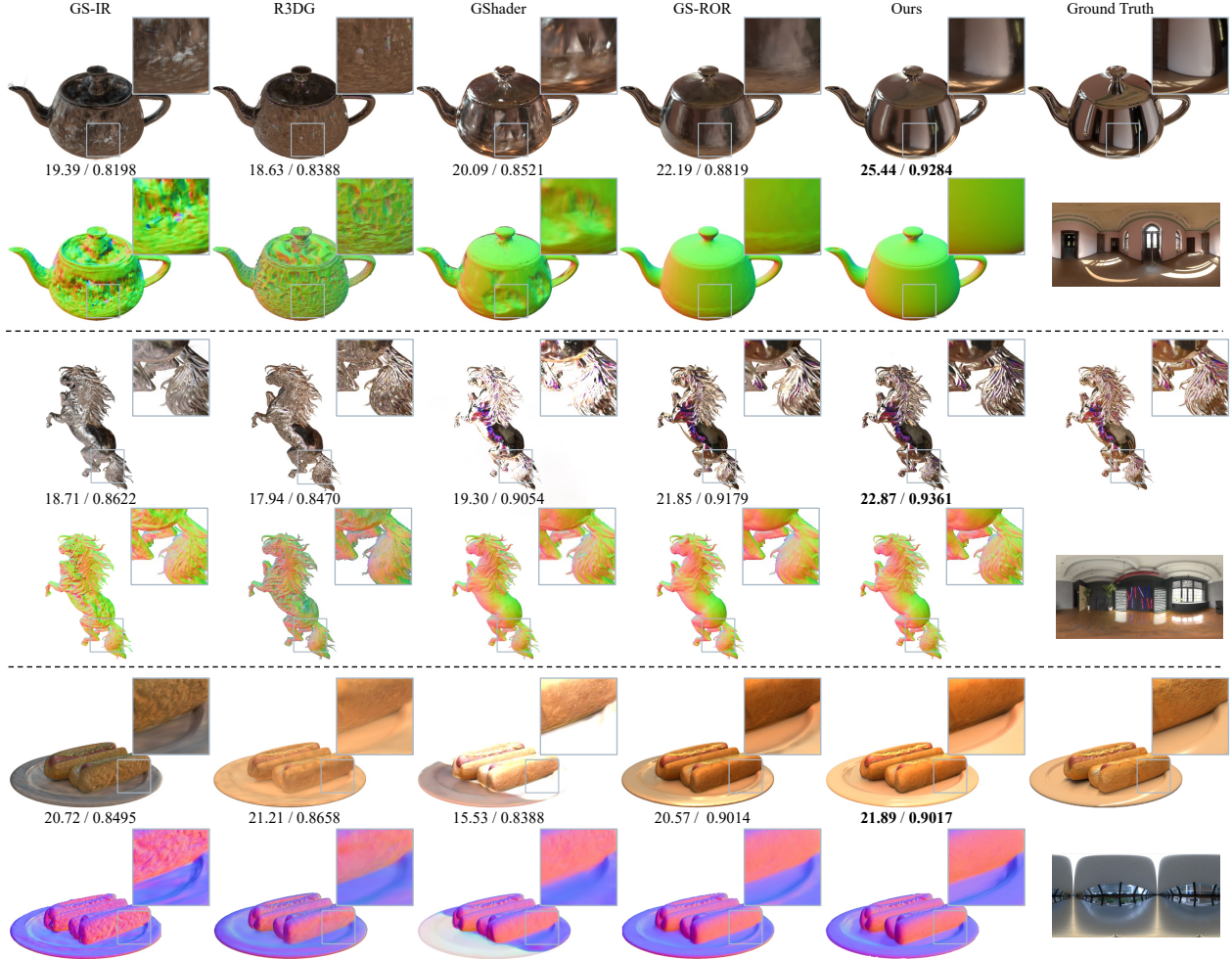


Figure 6. The comparison of relighting results and normal on the Glossy Blender (the 1st-4th rows) and the TensoIR synthetic dataset (the 5th, 6th rows). Our method provides reasonable normal robustly across materials, thus rendering realistic relighting results that include specular highlights. The PSNR/SSIM of relighting results under the current view are below images. More results are in the supplementary.

\mathcal{L}_γ and \mathcal{L}_p are our median and projection-based loss. More details are in the supplementary.

4.2. Evaluation setup

Dataset. We evaluate our method on three synthetic datasets, including TensoIR [10] synthetic dataset, Glossy Blender dataset [17] and Shiny Blender dataset. For real scenes, we select some objects from NeILF++ [37].

Methods for comparison. We select 4 representative Gaussian-based inverse rendering methods for comparison, including GShader [9], GS-IR [16], R3DG [6] and GS-ROR [44]. We trained these models based on their public codes and configurations with an extra mask loss for stabilizing training and fair comparison.

Metrics. We use the peak signal-to-noise ratio (PSNR) and structural similarity index (SSIM) [30], the learned perceptual image patch similarity (LPIPS) [40] to measure the relighting quality. Following NeRO and TensoIR, we rescale

the relighting images for quantitative evaluation. We compare the mean angular error (MAE) and the Chamber distance (CD) for geometry quality. We record the mean training time, the frame per second (FPS), and the memory usage during training on RTX 4090.

4.3. Comparison with previous methods

Relighting of synthetic objects. We evaluate the relighting performance of synthetic objects with various materials on the Glossy Blender and TensoIR synthetic datasets. The quantitative measurements are shown in Tab. 1 and Tab. 2. The relighting results with normal visualizations are in Fig. 6. Due to the robustness of decomposition, our method provides high-quality relighting results and smooth normal. In contrast, GS-IR, R3DG, and GShader overfit the training appearance, leading to erroneous normal. Regarding GS-ROR, it shows higher geometry quality, as it introduces a continuous SDF for regularization. However, the

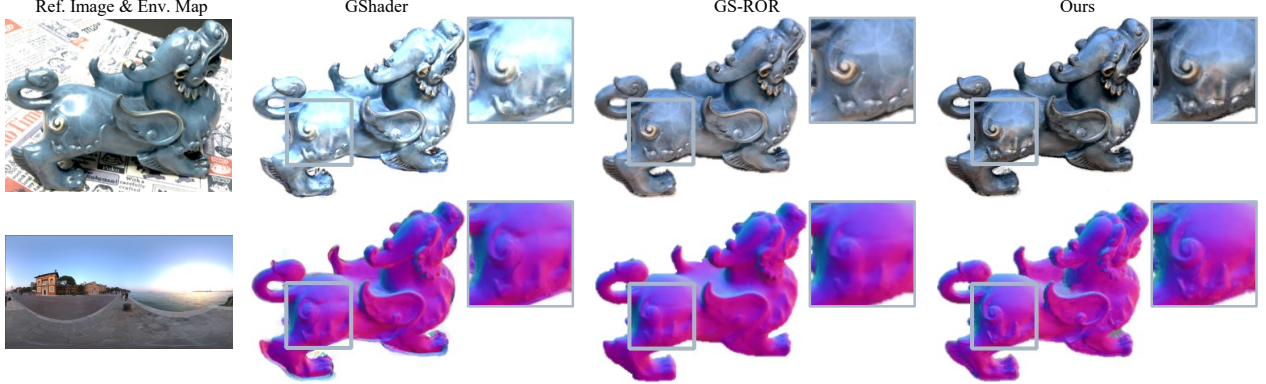


Figure 7. The qualitative comparison of relighting results and normal on the NeILF++ dataset. Our method can provide realistic relighting results and detailed normal for real data. More results are in the supplementary.

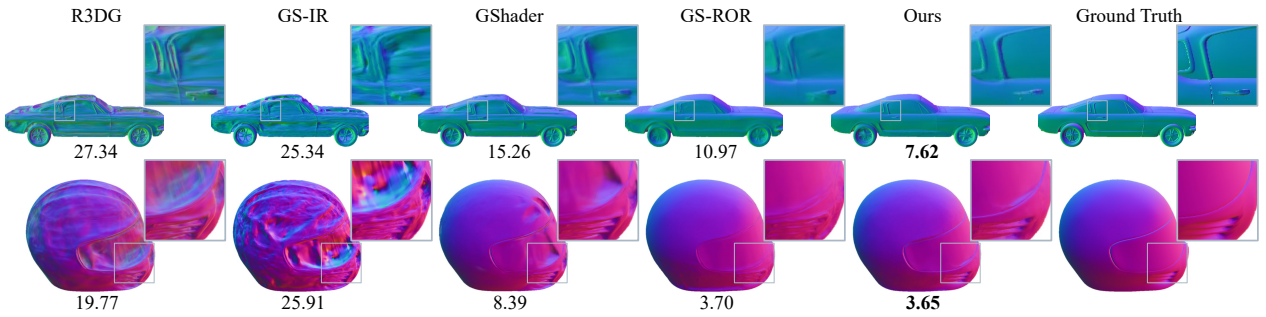


Figure 8. The qualitative comparison of normal on the Shiny Blender dataset. Our method provides globally smooth normal while preserving the sharp details. The MAE under the current view is below the visualization. More results are in the supplementary.

	GS-IR	R3DG	GShader	GS-ROR	Ours
Ball	25.79	22.44	7.03	0.92	1.20
Car	28.31	26.02	14.05	11.98	6.82
Coffee	15.38	13.39	14.93	12.24	11.42
Helmet	25.58	19.63	9.33	4.10	3.90
Teapot	15.35	9.21	7.17	5.88	5.02
Toaster	33.51	28.17	13.08	8.24	10.51
Mean	23.99	19.81	10.93	7.23	6.48

Table 3. Normal quality with Gaussian-based methods on Shiny Blender dataset in terms of $\text{MAE} \downarrow$. Numbers in red indicate the best performance and numbers in orange indicate the second best.

geometry details are lost in some regions, due to the difficulty in balancing two representations during training.

Relighting of real objects. The results of real scenes from NeILF++ are shown in Fig. 7. As ground truth is unavailable, we show reference training views and the results under novel light conditions.² Our method produces reasonable relighting results with sharp geometry details preserved.

Geometry quality. We compare reconstructed geometry quality in terms of normal MAE in Tab. 3 with the visualization in Fig. 8 and CD in Tab. 4.³ Numerically, our model outperforms all Gaussian-based inverse rendering

	GS-IR	R3DG	GShader	GS-ROR	Ours
Angel	0.0177	0.0098	0.0085	0.0063	0.0053
Bell	0.1153	0.0418	0.0110	0.0096	0.0094
Cat	0.0588	0.0339	0.0256	0.0222	0.0251
Horse	0.0196	0.0135	0.0073	0.0061	0.0052
Luyu	0.0225	0.0168	0.0107	0.0098	0.0106
Potion	0.0623	0.0380	0.0474	0.0146	0.0081
Tbell	0.1021	0.0500	0.0574	0.0270	0.0101
Teapot	0.0719	0.0479	0.0340	0.0166	0.0115
Mean	0.0588	0.0315	0.0253	0.0140	0.0107

Table 4. Surface quality with Gaussian-based methods on Glossy Blender dataset regarding $\text{CD} \downarrow$. Numbers in red indicate the best performance, and numbers in orange indicate the second best.

methods on most scenes and average metrics. However, our method fails in scenes with complex inter-reflection ('Toaster', 'Luyu', 'Cat') but still achieves sub-SOTA performance. Only GS-ROR succeeds in the scenes, at the cost of 5× of GPU memory usage than ours, due to their extra SDF network. Visually, our model **provides globally smooth normal (teapot in Fig. 6) and preserves local details (horse tail in Fig. 6)**, while GS-ROR *discards sharp details* and others *fail to reconstruct smooth surfaces*.

²R3DG, GS-IR do not converge on the scenes, thus no results provided.

³The choice of quantitative metrics depends on the available ground truth, and we use TSDF fusion [43] for surface extraction to evaluate CD.

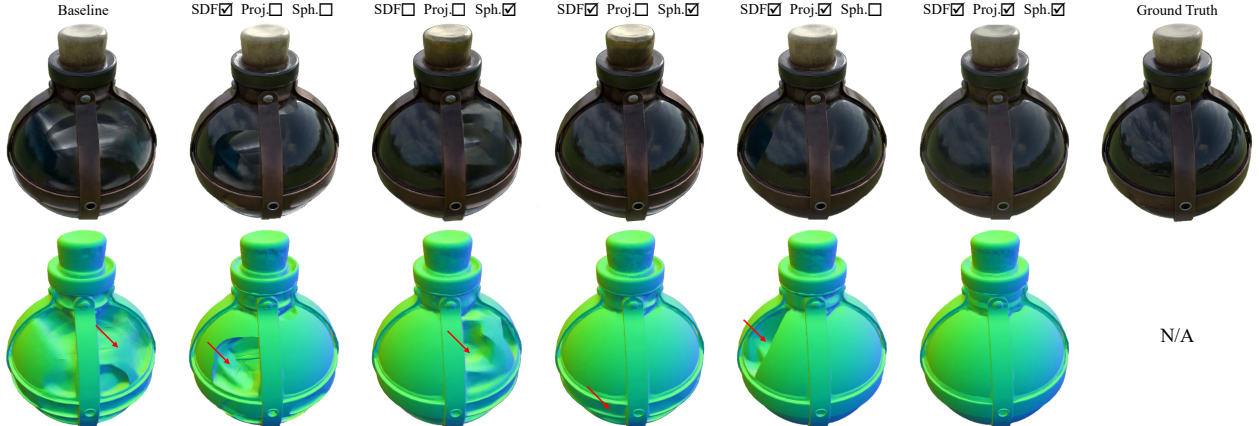


Figure 9. Ablation of the key components in our method on the Glossy Blender dataset, including the discretized SDF framework with the median loss, the projection-based consistency loss (Proj.), and spherical initialization (Sph.). (The red arrow points out the artifacts.)

Components			Scene			
SDF	Sph.	Proj.	Angel	Horse	Teapot	
			PSNR/SSIM	PSNR/SSIM	PSNR/SSIM	
✓			20.23/0.8533	20.72/0.8998	19.22/0.8674	
	✓		21.09/0.8815	22.13/0.9120	23.26/0.9223	
✓	✓		21.43/0.8881	21.96/0.9102	22.97/0.9176	
✓	✓	✓	21.59/0.8910	22.87/0.9284	23.45/0.9222	
✓	✓	✓	21.65/0.8917	23.21/0.9395	24.05/0.9289	
✓	✓	✓	22.03/0.8919	24.01/0.9481	24.19/0.9293	

Table 5. Ablation study of three key components on the Glossy Blender dataset. “SDF” means incorporating the discretized SDF with the median loss, “Proj.” means the projection-based consistency loss, and “Sph.” means the spherical initialization.

4.4. Ablation study

We conduct ablation studies of our main components on the Glossy Blender dataset, and the ablations of detailed choices (*e.g.*, losses, threshold) are in the supplementary. The quantitative results are in the Tab. 5. The performance of the model improves consistently when employing new components. We start from the baseline described in Sec. 3.2. As shown in the 1st column of Fig. 9, this baseline overfits the training appearance and fails to decompose geometry and material for relighting.

Discretized SDF with the median loss. Then, we incorporate the SDF-to-opacity transformation and the median loss that promotes the Gaussians converging to the opaque surface. As shown in the 2nd column of Fig. 9. The variant can decompose the material and geometry more robustly, thus improving the relighting quality. However, due to insufficient constraints, we still observe erroneous normal.

Projection-based consistency loss. Due to this loss is coupled with SDF, it cannot be ablated individually. Applying the projection-based consistency loss leads to more reasonable normal. However, erroneous geometry caused by misleading initialization still exists, as in the 5th row of Fig. 9.

Spherical initialization. The spherical initialization leads to performance increase with or without SDF designs (the 3rd, 4th, 6th columns of Fig. 9). However, applying it individually cannot ensure artifact-free results.

4.5. Discussion and limitations

In this work, we focus on improving the relighting quality by introducing SDF prior and leave mesh extraction with BRDF parameters for future work. Besides, we consider the direct lighting only for efficiency, so our method may fail for objects with complex occlusion. An extra indirect illumination term [6, 17] will further benefit our approach.

5. Conclusion

In this paper, we presented our Gaussian splatting framework for real-time object relighting, which regularizes the geometry from Gaussian primitives with a discretized SDF. In this framework, we proposed the median loss to facilitate the convergence and the projection-based consistency loss to constrain the discrete samples of SDF, along with the spherical initialization to avoid local minima. Therefore, our method benefits from the flexibility of GS and the robustness of SDF, thus outperforming the existing Gaussian-based inverse rendering methods in terms of relighting and decomposition quality, while maintaining simplicity and efficiency. In future work, extending our framework to unbounded scenes is a promising direction.

Acknowledgment: We thank the reviewers for the valuable comments. This work has been partially supported by the National Science and Technology Major Project under grant No. 2022ZD0116305, National Natural Science Foundation of China (NSFC) under grant No. 62172220, and the NSFC under Grant Nos. 62361166670 and U24A20330. Computation is supported by the Supercomputing Center of Nankai University.

References

- [1] Ma Baorui, Han Zhizhong, Liu Yu-Shen, and Zwicker Matthias. Neural-Pull: Learning signed distance functions from point clouds by learning to pull space onto surfaces. In *ICML*, 2021. 4
- [2] Sai Bi, Zexiang Xu, Pratul Srinivasan, Ben Mildenhall, Kalyan Sunkavalli, Miloš Hašan, Yannick Hold-Geoffroy, David Kriegman, and Ravi Ramamoorthi. Neural reflectance fields for appearance acquisition. *arXiv preprint arXiv:2008.03824*, 2020. 2
- [3] Mark Boss, Raphael Braun, Varun Jampani, Jonathan T. Barron, Ce Liu, and Hendrik P.A. Lensch. NeRD: Neural reflectance decomposition from image collections. In *ICCV*, pages 12684–12694, New York, NY, USA, 2021. IEEE. 2
- [4] Mark Boss, Varun Jampani, Raphael Braun, Ce Liu, Jonathan Barron, and Hendrik PA Lensch. Neural-PIL: Neural pre-integrated lighting for reflectance decomposition. In *NeurIPS*, pages 10691–10704, Red Hook, NY, USA, 2021. Curran Associates, Inc. 2
- [5] Hanlin Chen, Chen Li, and Gim Hee Lee. NeuSG: Neural implicit surface reconstruction with 3D Gaussian splatting guidance. *arXiv preprint arXiv:2312.00846*, 2023. 2
- [6] Jian Gao, Chun Gu, Youtian Lin, Zhihao Li, Hao Zhu, Xun Cao, Li Zhang, and Yao Yao. Relightable 3D Gaussians: Realistic point cloud relighting with BRDF decomposition and ray tracing. In *ECCV*, 2024. 2, 5, 6, 8
- [7] Amos Gropp, Lior Yariv, Niv Haim, Matan Atzmon, and Yaron Lipman. Implicit geometric regularization for learning shapes. In *ICML*. JMLR.org, 2020. 2
- [8] Binbin Huang, Zehao Yu, Anpei Chen, Andreas Geiger, and Shenghua Gao. 2D Gaussian splatting for geometrically accurate radiance fields. In *SIGGRAPH*, New York, NY, USA, 2024. Association for Computing Machinery. 3
- [9] Yingwenqi Jiang, Jiadong Tu, Yuan Liu, Xifeng Gao, Xiaoxiao Long, Wenping Wang, and Yuexin Ma. GaussianShader: 3D Gaussian splatting with shading functions for reflective surfaces. In *CVPR*, pages 5322–5332, New York, NY, USA, 2024. IEEE. 2, 6
- [10] Haian Jin, Isabella Liu, Peijia Xu, Xiaoshuai Zhang, Songfang Han, Sai Bi, Xiaowei Zhou, Zexiang Xu, and Hao Su. TensoIR: Tensorial inverse rendering. In *CVPR*, pages 165–174, New York, NY, USA, 2023. IEEE. 2, 6
- [11] Brian Karis. Real shading in unreal engine 4. *Proc. Physically Based Shading Theory Practice*, 2013. 3
- [12] Bernhard Kerbl, Georgios Kopanas, Thomas Leimkühler, and George Drettakis. 3D Gaussian splatting for real-time radiance field rendering. *ACM TOG*, 42(4):139–1, 2023. 2
- [13] Diederik P. Kingma and Jimmy Ba. Adam: A method for stochastic optimization. *arXiv preprint arXiv:1412.6980*, 2017. 5
- [14] Jia Li, Lu Wang, Lei Zhang, and Beibei Wang. TensoSDF: Roughness-aware tensorial representation for robust geometry and material reconstruction. *ACM TOG*, 43(4), 2024. 1, 2
- [15] Zhaoshuo Li, Thomas Müller, Alex Evans, Russell H. Taylor, Mathias Unberath, Ming-Yu Liu, and Chen-Hsuan Lin. Neuralangelo: High-fidelity neural surface reconstruction. In *CVPR*, pages 8456–8465, New York, NY, USA, 2023. IEEE. 2
- [16] Zhihao Liang, Qi Zhang, Ying Feng, Ying Shan, and Kui Jia. GS-IR: 3D Gaussian splatting for inverse rendering. In *CVPR*, pages 21644–21653, New York, NY, USA, 2024. IEEE. 2, 6
- [17] Yuan Liu, Peng Wang, Cheng Lin, Xiaoxiao Long, Jiepeng Wang, Lingjie Liu, Taku Komura, and Wenping Wang. NeRO: Neural geometry and BRDF reconstruction of reflective objects from multiview images. *ACM TOG*, 42(4), 2023. 1, 2, 6, 8
- [18] Xiaoyang Lyu, Yang-Tian Sun, Yi-Hua Huang, Xiuzhe Wu, Ziyi Yang, Yilun Chen, Jiangmiao Pang, and Xiaojuan Qi. 3DGSR: Implicit surface reconstruction with 3D Gaussian splatting. *ACM TOG*, 43(6), 2024. 2, 3
- [19] Daniel Mayost. Applications of the signed distance function to surface geometry. University of Toronto, 2014. 2, 4
- [20] Stephen McAuley, Stephen Hill, Adam Martinez, Ryusuke Villemin, Matt Pettineo, Dimitar Lazarov, David Neubelt, Brian Karis, Christophe Hery, Naty Hoffman, and Hakan Zap Andersson. Physically based shading in theory and practice. In *ACM SIGGRAPH 2013 Courses*, New York, NY, USA, 2013. Association for Computing Machinery. 3
- [21] Ben Mildenhall, Pratul P. Srinivasan, Matthew Tancik, Jonathan T. Barron, Ravi Ramamoorthi, and Ren Ng. NeRF: Representing scenes as neural radiance fields for view synthesis. In *ECCV*, pages 405–421, Berlin, Heidelberg, 2020. Springer. 1, 2
- [22] Radu Alexandru Rosu and Sven Behnke. PermuSDF: Fast multi-view reconstruction with implicit surfaces using permutohedral lattices. In *CVPR*, pages 8466–8475, New York, NY, USA, 2023. IEEE. 2
- [23] Yahao Shi, Yanmin Wu, Chenming Wu, Xing Liu, Chen Zhao, Haocheng Feng, Jingtuo Liu, Liangjun Zhang, Jian Zhang, Bin Zhou, Errui Ding, and Jingdong Wang. GIR: 3D Gaussian inverse rendering for relightable scene factorization. *arXiv preprint arXiv:2312.05133*, 2023. 2
- [24] Pratul P. Srinivasan, Boyang Deng, Xiuming Zhang, Matthew Tancik, Ben Mildenhall, and Jonathan T. Barron. NeRV: Neural reflectance and visibility fields for relighting and view synthesis. In *CVPR*, pages 7495–7504, New York, NY, USA, 2021. IEEE. 2
- [25] Cheng Sun, Guangyan Cai, Zhengqin Li, Kai Yan, Cheng Zhang, Carl Marshall, Jia-Bin Huang, Shuang Zhao, and Zhao Dong. Neural-PBIR reconstruction of shape, material, and illumination. In *ICCV*, pages 18046–18056, New York, NY, USA, 2023. IEEE. 1, 2
- [26] Dor Verbin, Peter Hedman, Ben Mildenhall, Todd Zickler, Jonathan T. Barron, and Pratul P. Srinivasan. Ref-NeRF: Structured view-dependent appearance for neural radiance fields. In *CVPR*, pages 5491–5500, New York, NY, USA, 2022. IEEE. 1
- [27] Haoyuan Wang, Wenbo Hu, Lei Zhu, and Rynson W.H. Lau. Inverse rendering of glossy objects via the neural plenoptic function and radiance fields. In *CVPR*, pages 19999–20008, New York, NY, USA, 2024. IEEE. 2

- [28] Peng Wang, Lingjie Liu, Yuan Liu, Christian Theobalt, Taku Komura, and Wenping Wang. NeuS: Learning neural implicit surfaces by volume rendering for multi-view reconstruction. In *NeurIPS*, pages 27171–27183, Red Hook, NY, USA, 2021. Curran Associates, Inc. [1](#), [2](#), [5](#)
- [29] Yiming Wang, Qin Han, Marc Habermann, Kostas Daniilidis, Christian Theobalt, and Lingjie Liu. NeuS2: Fast learning of neural implicit surfaces for multi-view reconstruction. In *ICCV*, pages 3295–3306, New York, NY, USA, 2023. IEEE. [2](#)
- [30] Zhou Wang, A.C. Bovik, H.R. Sheikh, and E.P. Simoncelli. Image quality assessment: from error visibility to structural similarity. *IEEE TIP*, 13(4):600–612, 2004. [6](#)
- [31] Zixiong Wang, Yunxiao Zhang, Rui Xu, Fan Zhang, Peng-Shuai Wang, Shuangmin Chen, Shiqing Xin, Wenping Wang, and Changhe Tu. Neural-singular-hessian: Implicit neural representation of unoriented point clouds by enforcing singular hessian. *ACM TOG*, 42(6), 2023. [2](#)
- [32] Tong Wu, Jia-Mu Sun, Yu-Kun Lai, Yuewen Ma, Leif Kobbelt, and Lin Gao. DeferredGS: Decoupled and editable Gaussian splatting with deferred shading. *arXiv preprint arXiv:2404.09412*, 2024. [2](#), [3](#)
- [33] Lior Yariv, Jiatao Gu, Yoni Kasten, and Yaron Lipman. Volume rendering of neural implicit surfaces. In *NeurIPS*, pages 4805–4815, Red Hook, NY, USA, 2021. Curran Associates, Inc. [2](#), [5](#)
- [34] Keyang Ye, Qiming Hou, and Kun Zhou. 3D Gaussian splatting with deferred reflection. In *SIGGRAPH*, New York, NY, USA, 2024. Association for Computing Machinery. [3](#)
- [35] Mulin Yu, Tao Lu, Linning Xu, Lihan Jiang, Yuanbo Xiangli, and Bo Dai. GSDF: 3DGs meets SDF for improved rendering and reconstruction. In *NeurIPS*, 2024. [2](#), [3](#)
- [36] Jingyang Zhang, Yao Yao, Shiwei Li, Tian Fang, David McKinnon, Yanghai Tsin, and Long Quan. Critical regularizations for neural surface reconstruction in the wild. In *CVPR*, pages 6270–6279, New York, NY, USA, 2022. IEEE. [2](#)
- [37] Jingyang Zhang, Yao Yao, Shiwei Li, Jingbo Liu, Tian Fang, David McKinnon, Yanghai Tsin, and Long Quan. NeILF++: Inter-reflectable light fields for geometry and material estimation. In *ICCV*, pages 3601–3610, New York, NY, USA, 2023. IEEE. [1](#), [6](#)
- [38] Kai Zhang, Fujun Luan, Qianqian Wang, Kavita Bala, and Noah Snavely. PhySG: Inverse rendering with spherical Gaussians for physics-based material editing and relighting. In *CVPR*, pages 5453–5462, New York, NY, USA, 2021. IEEE. [2](#), [5](#)
- [39] Kai Zhang, Fujun Luan, Zhengqi Li, and Noah Snavely. IRON: Inverse rendering by optimizing neural sdofs and materials from photometric images. In *CVPR*, pages 5565–5574, New York, NY, USA, 2022. IEEE. [2](#)
- [40] Richard Zhang, Phillip Isola, Alexei A. Efros, Eli Shechtman, and Oliver Wang. The unreasonable effectiveness of deep features as a perceptual metric. In *CVPR*, New York, NY, USA, 2018. IEEE. [6](#)
- [41] Wenyuan Zhang, Yu-Shen Liu, and Zhizhong Han. Neural signed distance function inference through splatting 3D Gaussians pulled on zero-level set. In *NeurIPS*, 2024. [2](#), [3](#)
- [42] Yuanqing Zhang, Jiaming Sun, Xingyi He, Huan Fu, Rongfei Jia, and Xiaowei Zhou. Modeling indirect illumination for inverse rendering. In *CVPR*, pages 18643–18652, New York, NY, USA, 2022. IEEE. [1](#), [2](#)
- [43] Qian-Yi Zhou, Jaesik Park, and Vladlen Koltun. Open3D: A modern library for 3d data processing. *arXiv preprint arXiv:1801.09847*, 2018. [7](#)
- [44] Zuo-Liang Zhu, Beibei Wang, and Jian Yang. GS-ROR: 3D Gaussian splatting for reflective object relighting via sdf priors. *arXiv preprint arXiv:2406.18544*, 2024. [2](#), [3](#), [6](#)

Gaussian Splatting with Discretized SDF for Relightable Assets

Supplementary Material

1. Model details

In this section, we complete the details of our model, including the losses, hyperparameters, shading model, and lighting model.

1.1. Loss details

We introduce the definition and weights of losses we used in the main paper. The color loss is defined as in 3DGS [4]

$$\mathcal{L}_c = \lambda \|C_{\text{gs}} - C_{\text{gt}}\|_1 + (1 - \lambda)(1 - \text{SSIM}(C_{\text{gs}}, C_{\text{gt}})), \quad (1)$$

where C_{gs} is the rendered color from Gaussians and C_{gt} is the ground truth color. The coefficient λ is set to 0.8. The supervision L_n from normal is defined as

$$\mathcal{L}_n = \|\hat{n} - n\|^2, \quad (2)$$

where \hat{n}, n are the normal from depth and the normal from Gaussians, respectively. We follow the 2DGS and apply the distortion loss as

$$\mathcal{L}_d = \sum_{i,j} w_i w_j |D_i - D_j|, \quad (3)$$

where w_i is the blending weight of i -th Gaussian and D_i is the intersection depth for the current pixel. The smoothness loss for BRDF parameters (*i.e.*, albedo \mathbf{a} , roughness \mathbf{r} , metallicity \mathbf{m}) is defined as

$$\mathcal{L}_{\text{sm}} = \|\nabla p\| \exp^{-\|\nabla C_{\text{gt}}\|}, (p \in \{\mathbf{a}, \mathbf{r}, \mathbf{m}\}) \quad (4)$$

where ∇ is the gradient operator and C_{gt} is the color of ground-truth image. The mask loss is the binary cross entropy between predicted and ground-truth masks. The corresponding weights for the above losses are shown in Tab. 1.

The learning rate of Gaussian attributes follows Gaussian Shader [1], except for the rate of SDF value (set to 0.05). The details of losses are present in the supplementary. The entire training takes about 1 hour on an RTX 4090.

1.2. Hyperparameters

As the median loss is used to promote convergence, we remove this loss when the SDF median $s_m < 0.2$, which indicates the transformation has been converged. Besides, the relaxing threshold ε for the projection-based consistency loss is set to 0.05. The number N for the spherical initialization is 10^6 .

Loss	\mathcal{L}_n	\mathcal{L}_d	\mathcal{L}_γ	\mathcal{L}_p	\mathcal{L}_{sm}	\mathcal{L}_m
Weight	0.2	2000	1	10	0.05	0.2

Table 1. The weights of losses present in the paper.

1.3. Split-sum approximation

A typical rendering equation needs to compute an integral on the upper hemisphere involving incident light, view direction, normal, and Bidirectional Reflectance Distribution Function (BRDF):

$$c(\omega_o) = \int_{\Omega} L_i(\omega_i) f(\omega_i, \omega_o) (\omega_i \cdot n) d\omega_i, \quad (5)$$

where $L_i(\omega_i)$ denotes the light from incident direction ω_i , $f(\omega_i, \omega_o)$ is the BRDF with respect to the incident direction ω_i and outgoing direction ω_o , and n denotes the surface normal. In practice, the Disney Principled BRDF [7] is the most widely used BRDF, consisting of a diffuse lobe and a specular lobe

$$f(\omega_i, \omega_o) = \underbrace{(1 - \mathbf{m}) \frac{\mathbf{a}}{\pi}}_{\text{diffuse}} + \underbrace{\frac{DFG}{4(\omega_i \cdot n)(\omega_o \cdot n)}}_{\text{specular}}, \quad (6)$$

where D is the normal distribution function, F is the Fresnel term, G is the geometry term, \mathbf{a} is the albedo, and \mathbf{m} is the metallicity. However, the integral is expensive to evaluate, and the split-sum technique [3] is an alternative widely used in real-time rendering. The specular term is approximated as

$$c_{\text{specular}} = L_{\text{specular}} \cdot ((1 - \mathbf{m}) \times 0.04 + \mathbf{m} \times \mathbf{a}) \times F_1 + F_2, \quad (7)$$

where F_1, F_2 are two scalars from a pre-computed table. The diffuse term is computed as

$$c_{\text{diffuse}} = \frac{\mathbf{a}(1 - \mathbf{m})}{\pi} \cdot L_{\text{diffuse}}. \quad (8)$$

L_{diffuse} and L_{specular} are directed queried for a pre-filtered environment map or neural light representations. The rendered color $c(\omega_o)$ is computed as

$$c(\omega_o) = c_{\text{diffuse}} + c_{\text{specular}}. \quad (9)$$

1.4. Lighting model

Considering the efficiency of the light query, we use a simple differential environment map and do not model the indirect illumination and occlusion. The environment light is in the cube map format, whose resolution is $6 \times 512 \times 512$.

	MII	TensoIR	TensoSDF	NeRO	Ours
	PSNR / SSIM / LPIPS				
Angel	16.24 / 0.8236 / 0.1404	10.24 / 0.2238 / 0.2739	20.40 / 0.8969 / 0.0871	16.21 / 0.7819 / 0.1923	22.03 / 0.8919 / 0.0819
Bell	17.41 / 0.8594 / 0.1534	10.11 / 0.1018 / 0.2806	29.91 / 0.9767 / 0.0263	31.19 / 0.9794 / 0.0189	24.67 / 0.9280 / 0.0842
Cat	17.68 / 0.8521 / 0.1429	9.10 / 0.1644 / 0.2146	26.12 / 0.9354 / 0.0675	28.42 / 0.9579 / 0.0455	26.48 / 0.9374 / 0.0661
Horse	20.98 / 0.8997 / 0.0713	10.42 / 0.1931 / 0.2913	27.18 / 0.9567 / 0.0318	25.56 / 0.9437 / 0.0410	24.01 / 0.9481 / 0.0351
Luyu	17.89 / 0.8050 / 0.1393	8.27 / 0.2375 / 0.2463	19.91 / 0.8825 / 0.0807	26.22 / 0.9092 / 0.0696	23.80 / 0.9017 / 0.0699
Potion	17.13 / 0.8094 / 0.1747	6.21 / 0.0846 / 0.2954	27.71 / 0.9422 / 0.0759	30.14 / 0.9561 / 0.0623	27.31 / 0.9280 / 0.0982
Tbell	16.54 / 0.8262 / 0.1938	7.47 / 0.1609 / 0.2786	23.33 / 0.9404 / 0.0543	25.45 / 0.9607 / 0.0407	23.66 / 0.9191 / 0.0981
Teapot	16.71 / 0.8546 / 0.1426	9.96 / 0.2093 / 0.2030	25.16 / 0.9482 / 0.0485	29.87 / 0.9755 / 0.0193	24.19 / 0.9293 / 0.0760
Mean	17.57 / 0.8413 / 0.1448	8.97 / 0.1719 / 0.2605	24.97 / 0.9349 / 0.0590	26.63 / 0.9331 / 0.0612	24.52 / 0.9229 / 0.0762
Training	4h	5h	6h	12h	1h
Ren. FPS	1/30	1/60	1/4	1/4	143
Memory	12G	23G	20G	8G	4G

Table 2. The quantitative comparison with NeRF-based methods on the Glossy Blender dataset in terms of PSNR↑, SSIM↑, and LPIPS↓. Numbers in red indicate the best performance, numbers in orange indicate the second best, and numbers in yellow indicate the third best. Although our method has a performance gap compared to NeRO and TensoSDF, our method is more efficient (at most **50% memory usage and 17% training time**).

	MII	NeRO	TensoSDF	TensoIR	Ours
	PSNR / SSIM / LPIPS				
Armad.	26.85 / 0.9441 / 0.0692	23.02 / 0.9335 / 0.0644	23.02 / 0.9355 / 0.0578	34.51 / 0.9754 / 0.0368	31.05 / 0.9621 / 0.0536
Ficus	20.65 / 0.9068 / 0.0728	27.43 / 0.9404 / 0.0677	28.53 / 0.9499 / 0.0533	24.32 / 0.9465 / 0.0543	27.85 / 0.9639 / 0.0390
Hotdog	22.65 / 0.9011 / 0.0893	20.45 / 0.9262 / 0.0888	20.47 / 0.9241 / 0.0906	27.92 / 0.9324 / 0.0833	26.23 / 0.9360 / 0.0746
Lego	23.20 / 0.8643 / 0.1715	17.76 / 0.8577 / 0.1228	17.92 / 0.8670 / 0.1088	27.61 / 0.9253 / 0.0702	25.81 / 0.9087 / 0.0791
Mean	23.34 / 0.9041 / 0.1007	22.17 / 0.9145 / 0.0859	22.48 / 0.9191 / 0.0776	28.59 / 0.9449 / 0.0612	27.78 / 0.9427 / 0.0626

Table 3. The quantitative comparison with NeRF-based methods on the TensoIR Synthetic dataset in terms of PSNR↑, SSIM↑, and LPIPS↓. Numbers in red indicate the best performance, numbers in orange indicate the second best, and numbers in yellow indicate the third best.

2. Proof of the projection-based loss

This part reveals how our projection-based consistency loss approximates the Eikonal loss.

Proposition 1. Consider a differentiable function f in the region Ω , for $\forall x_1 \in \Omega, f(x_1) \neq 0$ and its projection point $x_0 = x_1 - \nabla f(x_1)/|\nabla f(x_1)| \cdot f(x_1)$, if we guarantee x_0 on the surface ($f(x_0) = 0$), the Eikonal condition $|\nabla f(x)| = 1$ can be approximated at least in a narrow thin-shell space surrounding the surface.

Proof. The Taylor expansion of f at position x_1 is

$$f(x) = f(x_1) + \nabla f(x_1)(x - x_1) + O((x - x_1)^2) \quad (10)$$

where $\nabla f(x_1)$ means the gradient of f at x_1 and $O((x - x_1)^2)$ means the higher-order term of f . Then substitute x_0 into $f(x)$:

$$\begin{aligned} x_0 - x_1 &= -f(x_1) \cdot \nabla f(x_1)/|\nabla f(x_1)|, \\ f(x_0) &= f(x_1) - f(x_1) \frac{\nabla f(x_1)^2}{|\nabla f(x_1)|} + O((x_0 - x_1)^2) \quad (11) \\ f(x_1)(1 - |\nabla f(x_1)|) + O((x_0 - x_1)^2) &= 0 \end{aligned}$$

	GS-ROR	Ours w/o mask	Ours w/ mask
	PSNR / SSIM	PSNR / SSIM	PSNR / SSIM
Angel	20.81 / 0.8775	21.03 / 0.8842	22.03 / 0.8919
Horse	23.31 / 0.9376	23.35 / 0.9406	24.01 / 0.9481
Teapot	21.17 / 0.8932	22.57 / 0.9087	24.19 / 0.9293

Table 4. The impact of the mask loss on our method.

which means $|\nabla f(x)| = 1$ is approximated for each x_1 where x_0, x_1 is close enough to make the high-order term $O((x_0 - x_1)^2)$ negligible. Therefore, we can guarantee the Eikonal condition near the surface where Gaussians exist.

3. More results

In this section, we present the ablation of detailed choices in our model and more results of our method. Additionally, we select some representative NeRF-based methods for further validation, including MII [10], TensoIR [2], TensoSDF [5], and NeRO [6].

ε	0.01	0.05	0.1	0.2
	PSNR / SSIM	PSNR / SSIM	PSNR / SSIM	PSNR / SSIM
Angel	21.78 / 0.8860	21.91 / 0.8880	22.03 / 0.8919	21.54 / 0.8769
Horse	22.10 / 0.9214	22.51 / 0.9317	24.01 / 0.9481	20.12 / 0.9220
Teapot	23.28 / 0.9190	23.84 / 0.9232	24.19 / 0.9293	23.37 / 0.9200

Table 5. Ablation study on the threshold ε in our method.

Iterations	7K		15K		30K	
	PSNR / SSIM	PSNR / SSIM	PSNR / SSIM	PSNR / SSIM	PSNR / SSIM	PSNR / SSIM
No reg.	17.96 / 0.8881		22.13 / 0.9175		22.82 / 0.9330	
$\gamma = \gamma_m$	18.85 / 0.9032		22.46 / 0.9239		22.91 / 0.9332	
\mathcal{L}_γ	22.20 / 0.9221		23.64 / 0.9319		24.19 / 0.9481	

Table 6. Ablation study on the median loss \mathcal{L}_γ in our method. “No reg.” means imposing no regularization on the transformation.

	GS-IR PSNR / CD	GShader PSNR / CD	R3DG PSNR / CD	GS-ROR PSNR / CD	Ours PSNR / CD
Ball	18.30 / —	30.40 / —	21.39 / —	35.50 / —	34.64 / —
Car	25.30 / 0.61	28.39 / 0.26	26.59 / 0.23	30.52 / 0.17	30.55 / 0.14
Coffee	30.72 / 1.22	30.79 / 1.05	32.57 / 1.14	30.79 / 1.51	32.91 / 0.92
Helmet	25.08 / 1.22	26.95 / 1.09	28.78 / 1.31	32.62 / 0.23	30.06 / 0.15
Toaster	18.66 / 0.72	23.95 / 0.75	20.07 / 0.80	25.89 / 0.53	25.02 / 0.68
Teapot	38.21 / —	43.35 / —	43.86 / —	43.88 / —	43.39 / —

Table 7. Comparison in terms of PSNR and CD \downarrow ($\times 100$).

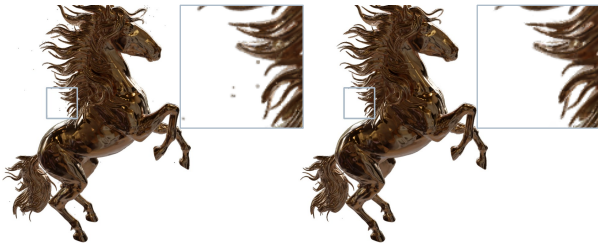


Figure 1. Without the projection-based consistency loss, we observe the artifacts caused by outliers (left). The loss encourages the outlier towards the surface, thus diminishing the artifacts.

3.1. Extra ablation studies

We ablate our hyperparameter choice and loss usage in this part, including the threshold in the projection-based loss, the impact of the median and the mask loss.

The choice of the threshold ε . A large threshold forces Gaussians onto wrong surfaces, while a small one causes most Gaussians to be excluded, resulting in decreased performance. Therefore, we choose to set $\varepsilon = 0.1$ for all scenes, which reveals its generalization ability and yields the best performance in Tab. 5.

The impact of the median loss. We use the median loss to encourage γ towards γ_m , instead of directly setting $\gamma = \gamma_m$, because γ_m is used to give the direction of optimization and not the target. Besides, the median loss enables the further optimization of the transformation. Our experiment also proves that the median loss promotes the convergence

while others variants fail, as shown in Tab. 6. Besides, the setting of $\mathcal{T}_{\gamma_m}(|s|_m) = o_m = 0.5$ is from our observation, as larger γ_m values cause early over-pruning of Gaussians, while smaller values fail to narrow the transformation. Both cases reduce performance.

The impact of the mask loss. While removing the mask loss leads to a performance decrease of 1dB, it still outperforms GS-ROR trained with the mask loss, as shown in Tab. 4.

3.2. Extra benefits from the projection-based loss

Our projection loss also promotes the Gaussian outliers moving toward the surface and diminishes the artifacts, as shown in Fig. 1.

3.3. Glossy Blender dataset

We present the relighting results with the decomposition of material and geometry on the Glossy Blender dataset [6] in Fig. 2. As there is no material ground truth, we only provide the visualization of our method. More qualitative comparisons are in Fig. 3. Our method offers smooth geometry with details preserved and thus outperforms other Gaussian-based methods regarding relighting quality. Besides, we compare our method with four NeRF-based inverse rendering methods in Tab. 2, and our method is still competitive. MII and TensoIR do not design for reflective surfaces and thus perform poorly on the Glossy dataset. Although our method has a performance gap compared to NeRO and TensoSDF, our method is far more efficient than theirs with 50% memory usage and 17% training time at most. Our method also supports real-time rendering while other NeRF-based methods fail¹. Besides, as shown in Fig. 4, the results from our methods include sharp details that other NeRF-based methods fail to reconstruct and thus are more visually realistic.

3.4. Shiny Blender dataset

We present the decomposition of material and geometry with the relighting results on the Shiny Blender dataset [8] in Fig. 5. Due to no relighting ground truth, we show the environment map for shading as the reference. Besides, we present more qualitative comparisons of normal in Fig. 6. Due to the robustness of our method, our method provides high-quality relighting results for reflective surfaces. Additionally, We present the evaluation of surface quality in terms of Chamber distance (CD) along with NVS results in Tab. 7. Our method outperforms other methods in terms of CD, while GS-ROR achieves a higher quality than ours in some cases. The main reason is that our backbone is 2DGS

¹NeRO and TensoSDF use the Cycles Render Engine in Blender to provide relighting results, so the FPS depends on samples per pixel, which is 1024 following the NeRO setting.

while theirs is 3DGS. Although 2DGS demonstrates superior reconstruction quality, its NVS quality is lower compared to that of 3DGS.

3.5. TensoIR synthetic dataset

We present the decomposition of material and geometry on the TensoIR synthetic dataset [2] in Fig. 7. Besides, we present more qualitative comparisons of normal in Fig. 8. Our method provides a reasonable decomposition for diffuse objects and realistic relighting results. The quantitative comparison between our method and NeRF-based methods is shown in Tab. 3, and the qualitative comparison between our method and NeRF-based methods is Fig. 9. Our method is numerically and visually competitive for diffuse object relighting while maintaining efficiency.

3.6. NeILF++ dataset

We present more comparisons between our method and other Gaussian-based inverse rendering methods on the NeILF++ [9] dataset, revealing the robustness of our method for real-world objects. As shown in Fig. 10, our method provides realistic relighting results and detailed normal for diverse real objects.

References

- [1] Yingwenqi Jiang, Jiadong Tu, Yuan Liu, Xifeng Gao, Xiaoxiao Long, Wenping Wang, and Yuexin Ma. GaussianShader: 3D Gaussian splatting with shading functions for reflective surfaces. In *CVPR*, pages 5322–5332, New York, NY, USA, 2024. IEEE. 1
- [2] Haian Jin, Isabella Liu, Peijia Xu, Xiaoshuai Zhang, Songfang Han, Sai Bi, Xiaowei Zhou, Zexiang Xu, and Hao Su. TensoIR: Tensorial inverse rendering. In *CVPR*, pages 165–174, New York, NY, USA, 2023. IEEE. 2, 4
- [3] Brian Karis. Real shading in unreal engine 4. *Proc. Physically Based Shading Theory Practice*, 2013. 1
- [4] Bernhard Kerbl, Georgios Kopanas, Thomas Leimkühler, and George Drettakis. 3D Gaussian splatting for real-time radiance field rendering. *ACM TOG*, 42(4):139–1, 2023. 1
- [5] Jia Li, Lu Wang, Lei Zhang, and Beibei Wang. TensoSDF: Roughness-aware tensorial representation for robust geometry and material reconstruction. *ACM TOG*, 43(4), 2024. 2
- [6] Yuan Liu, Peng Wang, Cheng Lin, Xiaoxiao Long, Jiepeng Wang, Lingjie Liu, Taku Komura, and Wenping Wang. NeRO: Neural geometry and BRDF reconstruction of reflective objects from multiview images. *ACM TOG*, 42(4), 2023. 2, 3
- [7] Stephen McAuley, Stephen Hill, Adam Martinez, Ryusuke Villemin, Matt Pettineo, Dimitar Lazarov, David Neubelt, Brian Karis, Christophe Hery, Naty Hoffman, and Hakan Zap Andersson. Physically based shading in theory and practice. In *ACM SIGGRAPH 2013 Courses*, New York, NY, USA, 2013. Association for Computing Machinery. 1
- [8] Dor Verbin, Peter Hedman, Ben Mildenhall, Todd Zickler, Jonathan T. Barron, and Pratul P. Srinivasan. Ref-NeRF: Structured view-dependent appearance for neural radiance fields. In *CVPR*, pages 5491–5500, New York, NY, USA, 2022. IEEE. 3
- [9] Jingyang Zhang, Yao Yao, Shiwei Li, Jingbo Liu, Tian Fang, David McKinnon, Yanghai Tsin, and Long Quan. NeILF++: Inter-reflectable light fields for geometry and material estimation. In *ICCV*, pages 3601–3610, New York, NY, USA, 2023. IEEE. 4
- [10] Yuanqing Zhang, Jiaming Sun, Xingyi He, Huan Fu, Rongfei Jia, and Xiaowei Zhou. Modeling indirect illumination for inverse rendering. In *CVPR*, pages 18643–18652, New York, NY, USA, 2022. IEEE. 2

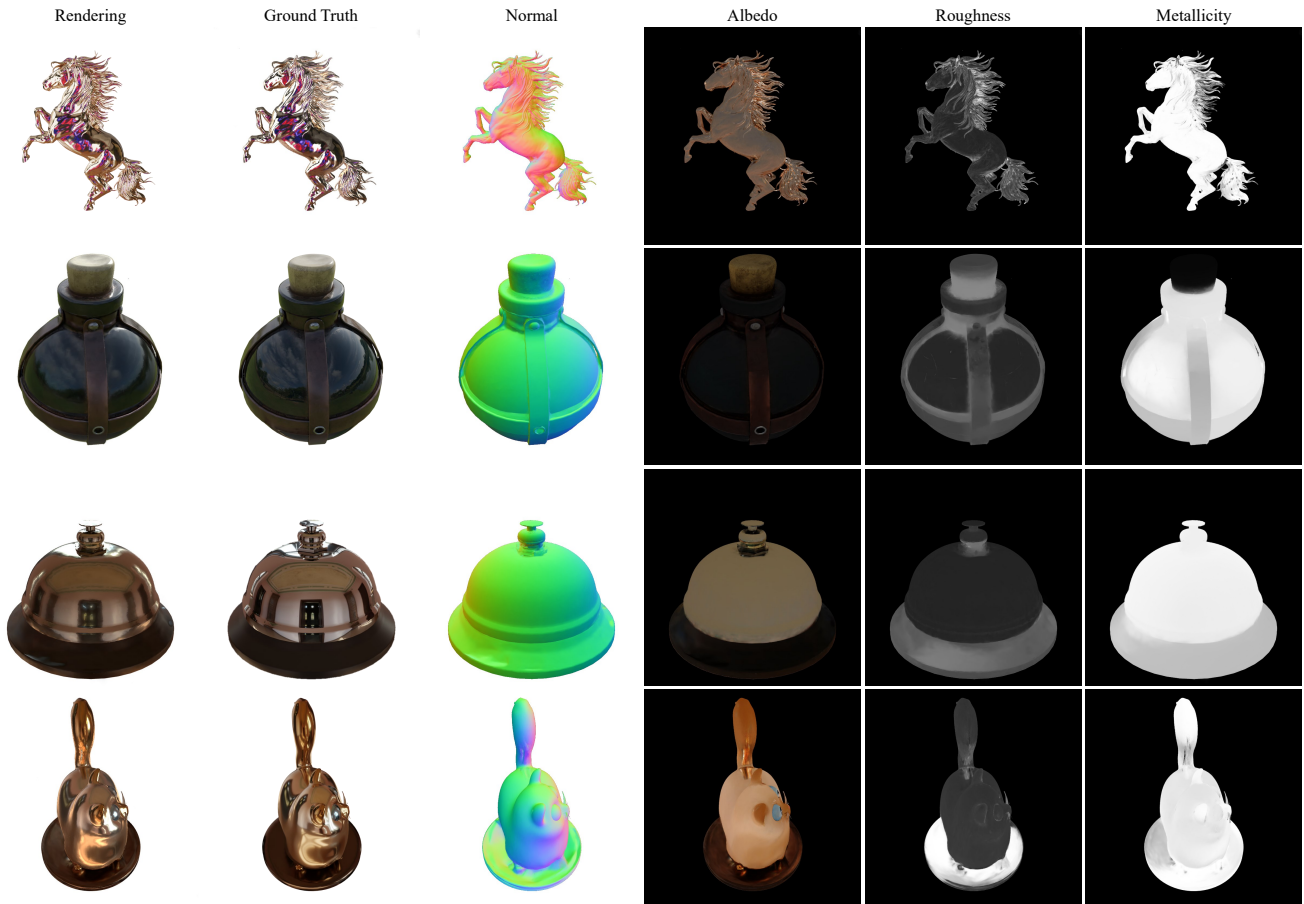


Figure 2. Decomposed maps of our method on the Glossy Blender dataset. Our method can provide a reasonable decomposition for reflective surfaces.

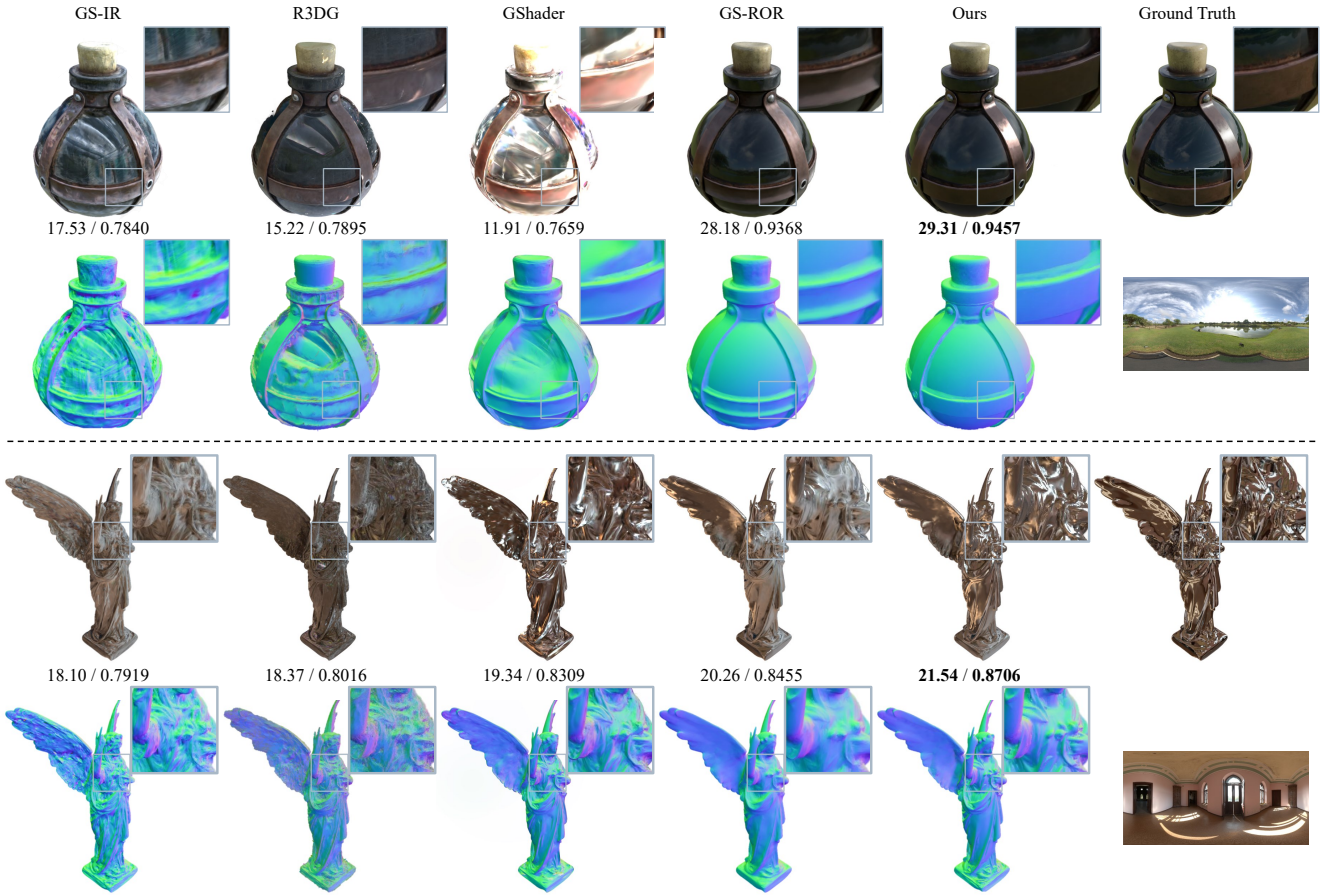


Figure 3. The qualitative comparison with Gaussian-based methods in terms of relighting results and normal on the Glossy Blender dataset. Our method provides high-quality relighting results for reflective surfaces. The PSNR/SSIM of relighting results under the current view are below the images.

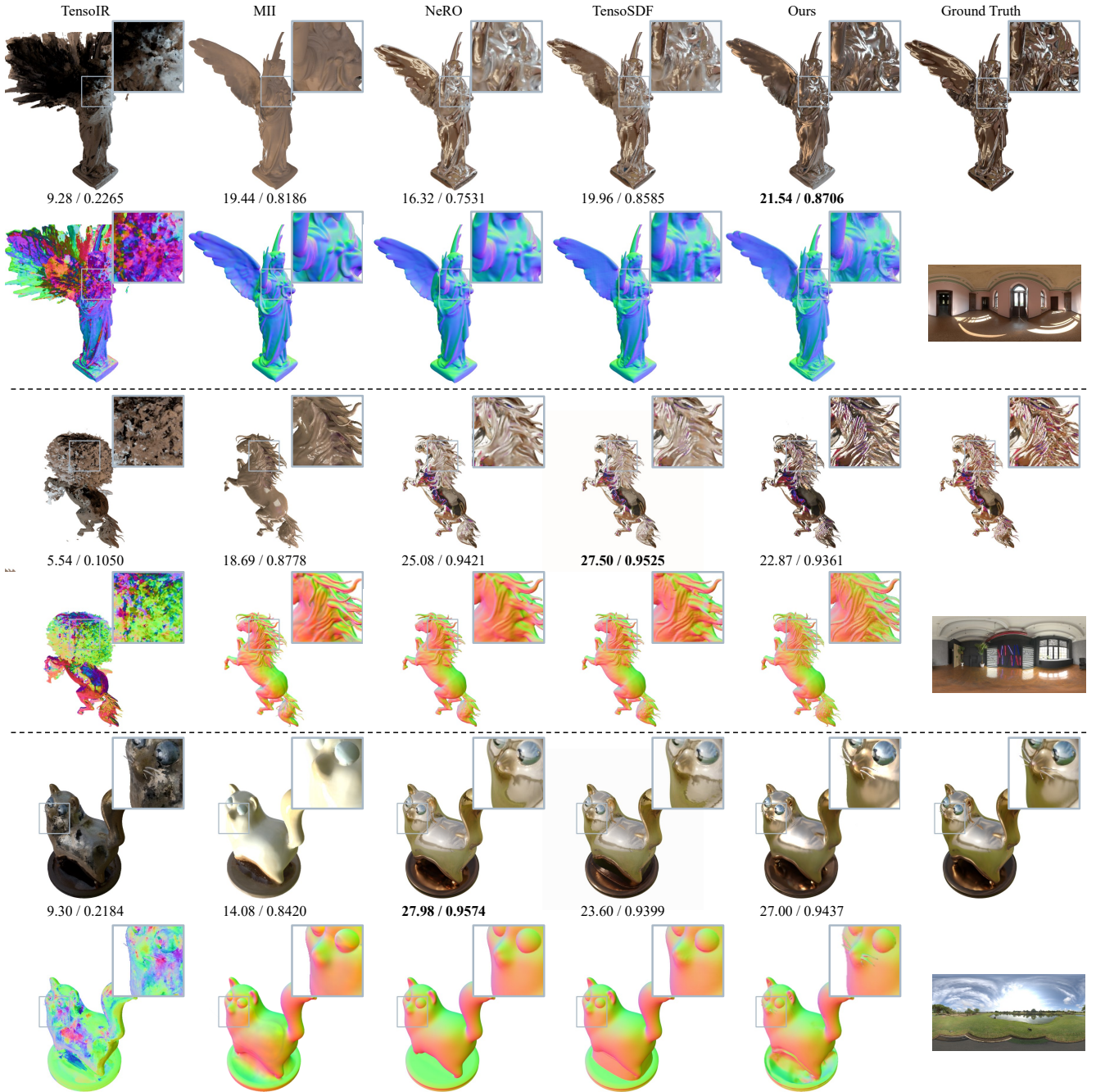


Figure 4. The qualitative comparison with NeRF-based methods in terms of relighting results and normal on the Glossy Blender dataset. Our method is competitive with these methods and outperforms in the detailed regions. The PSNR/SSIM of relighting results under the current view are below the images.

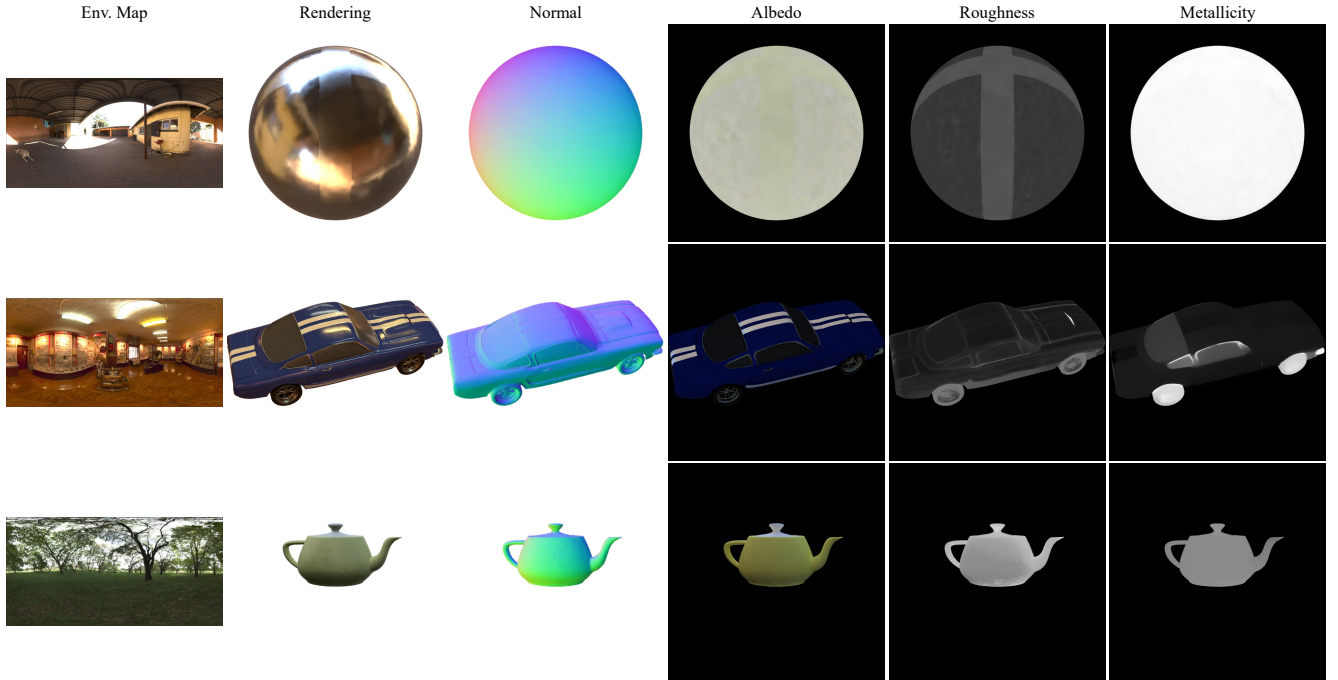


Figure 5. Decomposed maps of our method on the Shiny Blender dataset. The relighting ground truth is unavailable on the dataset, so we provide the environment map for shading as a reference.

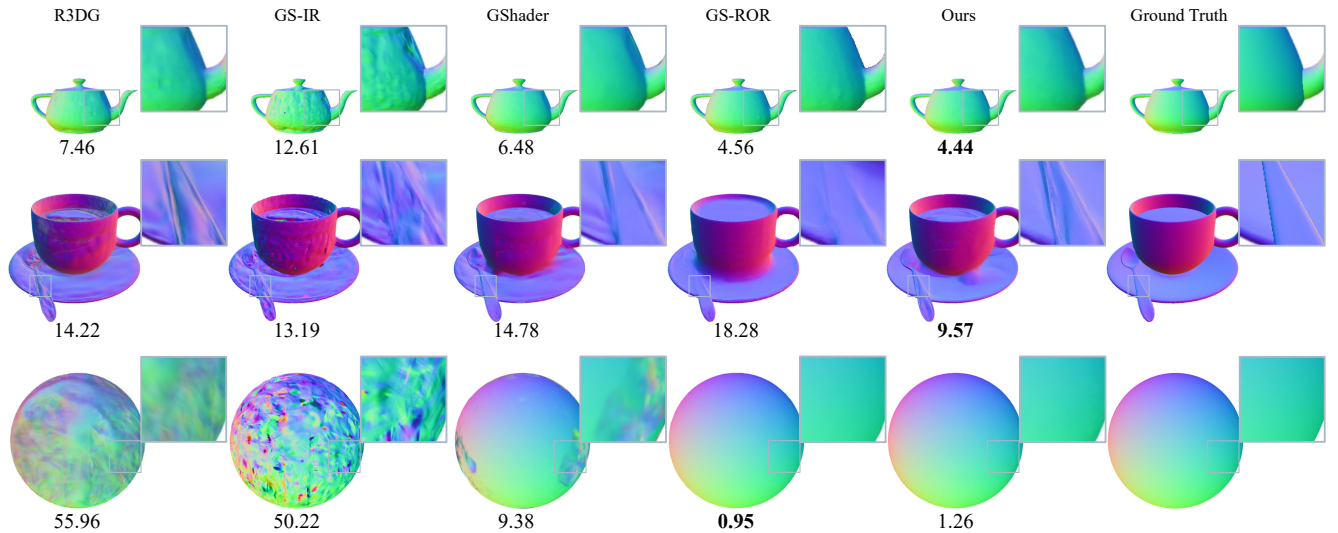


Figure 6. The qualitative comparison with Gaussian-based methods in terms of normal on the Shiny Blender dataset. The MAE under the current view is above the visualization. Our method can provide reasonable normal for diverse objects.

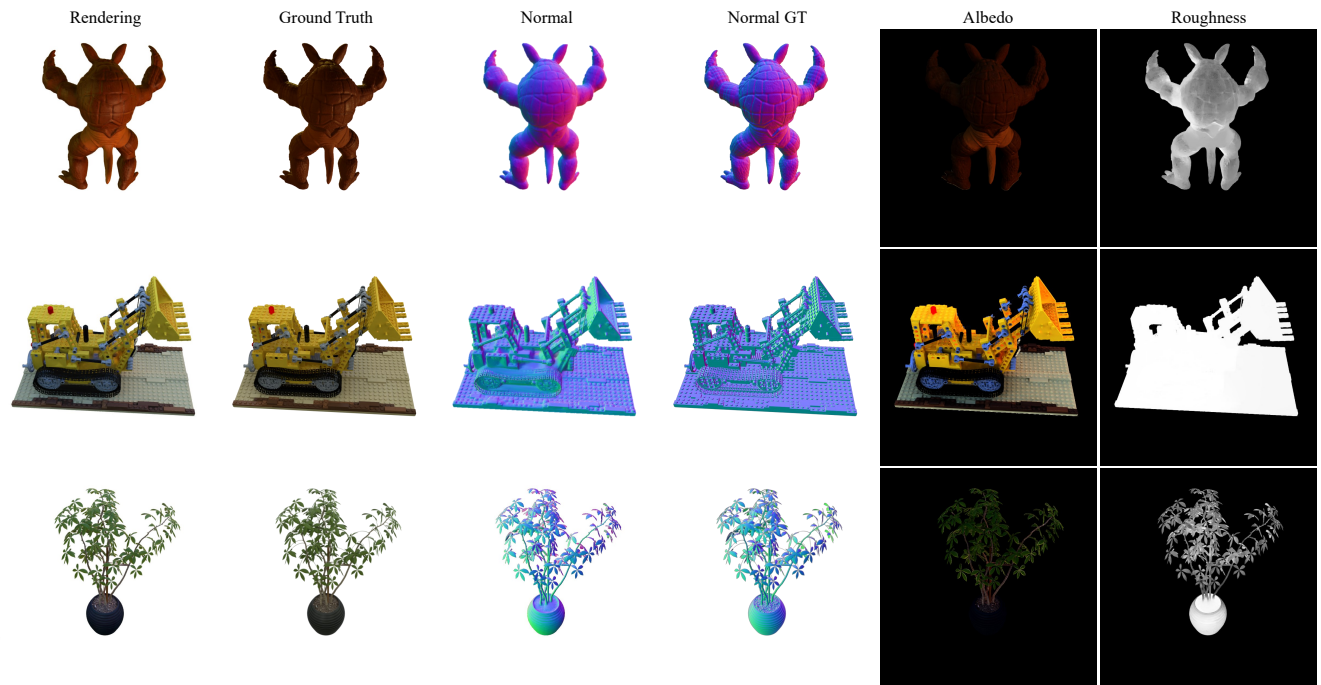


Figure 7. Decomposed maps of our method on the TensoIR synthetic dataset. Our method can provide a reasonable decomposition for diffuse objects.

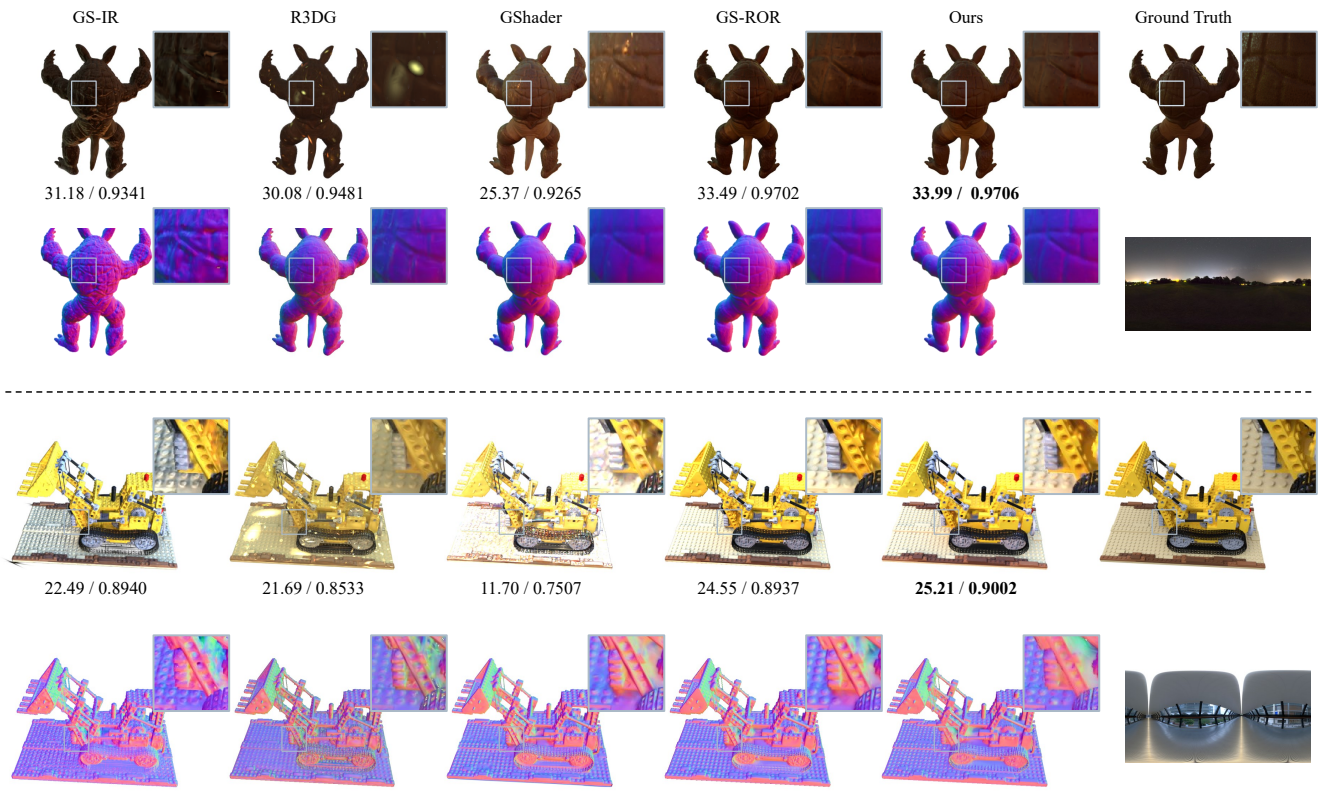


Figure 8. The qualitative comparison with Gaussian-based methods in terms of relighting results and normal on the TensoIR synthetic dataset. Our method can provide robust normal for diffuse objects. The PSNR/SSIM of relighting results under the current view are below the images.

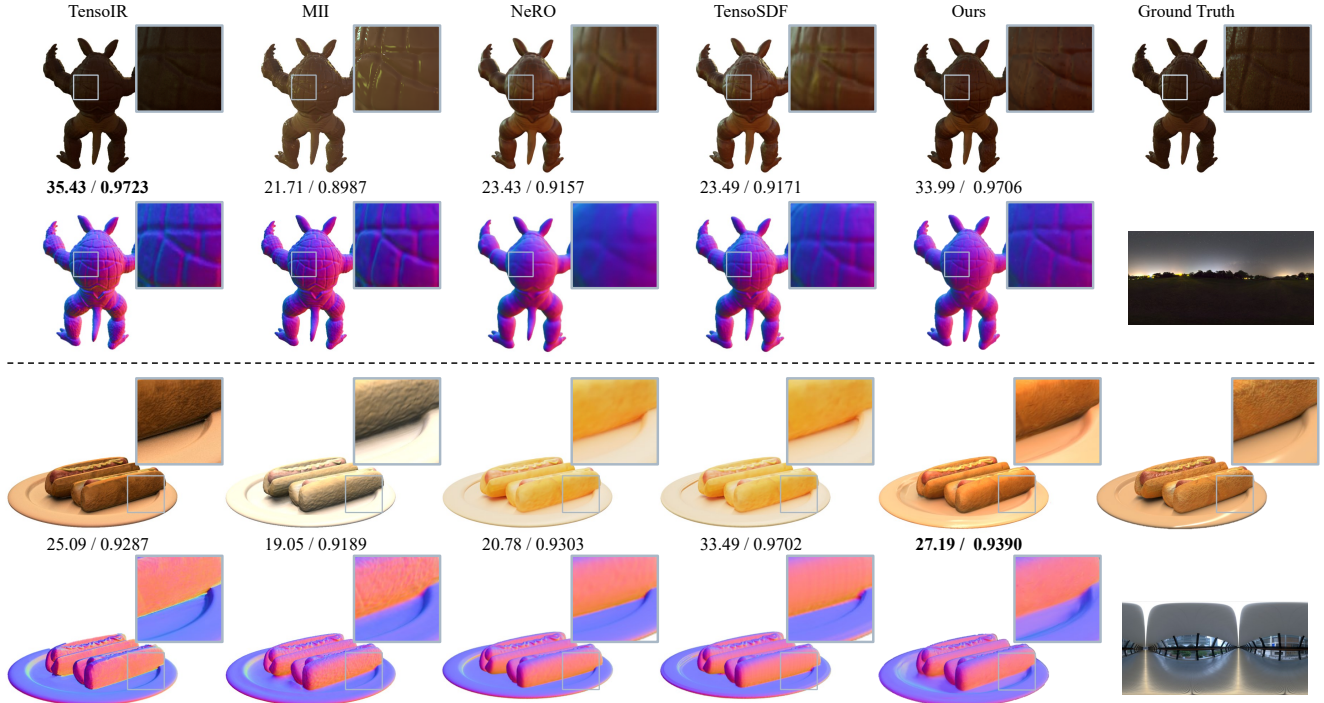


Figure 9. The qualitative comparison with NeRF-based methods in terms of relighting results and normal on the TensoIR synthetic dataset. Our method is competitive while maintaining high efficiency. The PSNR/SSIM of relighting results under the current view are below the images.



Figure 10. The qualitative comparison in terms of relighting results and normal on the NeILF++ dataset. Our method ensures the smoothness of normal while preserving details for real data, thus providing more realistic relighting results.